Accurate modelling of the elastic behavior of a continuum with the Discrete Element Method

M.A. Celigueta[1,2], S. Latorre[1], F. Arrufat[1] and E. Oñate[1,2]

[1] *Centre Internacional de Metodes Numerics a l'Enginyeria - CIMNE*
[2] *Universitat Politècnica de Catalunya (UPC)*
08034 Barcelona, Spain

Abstract

The Discrete Element Method (DEM) has been used for modeling continua, like concrete or rocks. However, it requires a big calibration effort, even to capture just the linear elastic behavior of a continuum modelled via the classical force-displacement relationships at the contact interfaces between particles. In this work we propose a new way for computing the contact forces between discrete particles. The newly proposed forces take into account the surroundings of the contact, not just the contact itself. This brings in the missing terms that provide an accurate approximation to an elastic continuum, and avoids calibration of the DEM parameters for the purely linear elastic range.

Keywords: DEM, Continuum, Elasticity, Young's modulus, Poisson's ratio

1. Introduction

The Discrete Element Method (DEM) has proven to be a very useful tool for the numerical computation of granular flows [1, 2, 3] (the hereafter termed non-cohesive DEM) with or without coupling with fluids [4, 5] or structures [6]. These computations can include cohesive forces between particles [7] to model moisture, glue or other added features to the standard non-cohesive DEM. Other research lines have focused on the DEM as a method to compute the mechanics of strongly cohesive materials, like rocks, concrete or cement [8, 9, 18], and it has been combined with the Finite Element Method in order to save computation time [19]. The approach in these cases is usually termed under the name of 'bonded' or cohesive DEM. Here the DEM can be understood as a discretization method for the continuum. The ability of the DEM to reproduce multi-cracking phenomena in those cohesive materials is probably one of the main reasons why the DEM is chosen. However, a moderately deep analysis of the works published usually reveals a lack of accuracy of the DEM results in the elastic regime, together with

a strong need for calibrating the DEM parameters. In particular, the Poisson's ratio and the shear modulus are seldom validated and it is commonly accepted [10] that the Poisson's ratio has a strong dependency on the mesh arrangement and on the ratio k_t/k_n [11], where k_n and k_t are the normal and tangential spring stiffness, respectively, in the spring dash-pot model that yields the forces at the contact interface between two spheres. The difficulty of the 'bonded' DEM to get accurate results when trying to capture simultaneously the Young's modulus (E), the Poisson's ratio (ν) and the shear modulus (G) derives from the fact that the bonded DEM works as a system of trusses instead of a massive continuum. Usually, a good calibration of the micro parameters (k_n and k_t) leads to a decent capture of one or two of the elastic macro parameters (E, G and ν) for a given mesh arrangement and usually for a certain, limited, range of values [11]. Due to these limitations, the spring dash-pot model has proven not to be good enough to capture the elastic behavior of a continuum. In this work we propose a way to enrich the spring dash-pot model in such a way that the elastic properties of a continuum can be accurately captured with the DEM.

2. Objectives

The objectives of this work are:

1. Modify the way the forces between pairs of spheres are computed in the DEM so an elastic continuum can be modelled accurately.
2. Provide the necessary equations so that the calibration of the micro parameters for the DEM is not needed for accurately reproducing the elastic behavior of a continuum.
3. Ensure that the DEM solution is independent from the size of the spheres, the granulometry of the material, the coordination number (the average number of particle neighbors) or the type of particle arrangement (cartesian, dense packing, random, etc.).

3. Computation of the elastic forces between particles

3.1. Normal forces

Since the main goal is to reproduce the elasticity of a continuum, the initial step to deduce the inter-particle forces is to analyze in detail the strain-stress constitutive equations:

$$\varepsilon_i = \frac{\sigma_i}{E} - \frac{\nu}{E}(\sigma_j + \sigma_k) \tag{1}$$
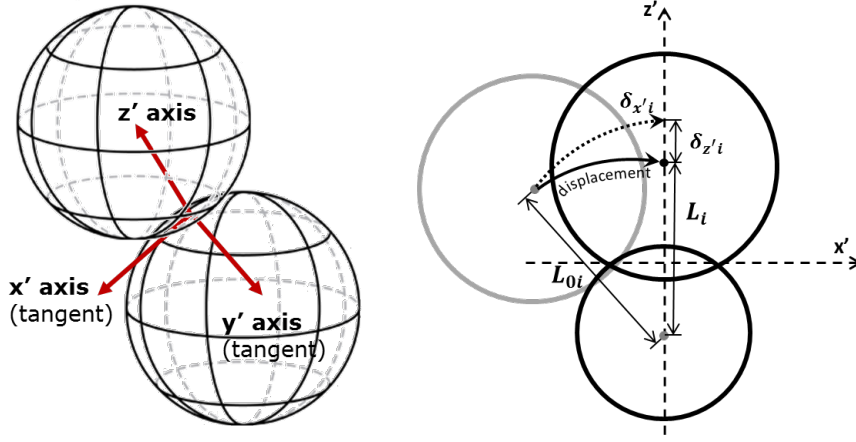
$$\gamma_{ij} = \frac{\tau_{ij}}{G} \tag{2}$$

Figure 1: Schematic definition of local axes at a contact point i between two spheres. a) Stress-free position. b) Deformed position

where E, G and ν are the Young's modulus, the shear modulus and the Poisson's ratio, respectively, and i, j, k are the cyclic permutation of the Cartesian coordinates x, y, z.

Sub-indices i, j, k denote generally the Cartesian axes. Without lack of generality it can be assumed that Eqs.(1) and (2) also hold if we choose $i = z'$, $j = x'$ and $k = y'$, where the primes denote the local axes at a contact point between two particles (Figure 1a). For simplicity we will assume in this work that the DEM particles are spherical. However, the method can be easily generalized to any particle shape.

In order to get the normal force between two spheres contacting at a point i, we can isolate $\sigma_{z'}$ from Eq.(1) to get:

$$\sigma_{z'i} = E\varepsilon_{z'i} + \nu(\sigma_{x'i} + \sigma_{y'i}) \tag{3}$$

where subindex i refers to the ith contact point.

The next step is to substitute $\sigma_{z'i}$ and $\varepsilon_{z'i}$ in Eq.(3) in terms of the interface forces and elongations. Namely,

$$\frac{F_{z'_i}}{A_i} = E\frac{\delta_{z'i}}{L_{0i}} + \nu(\sigma_{x'i} + \sigma_{y'i}) \tag{4}$$

where $F_{z'_i}$ is the force between the two particles in the normal direction z' (defined by the vector that joins the particle centers), A_i is the contact area at the ith contact interface between the two particles, L_{0i} is the distance between the centers of the particles at the stress-free position and $\delta_{z'i}$ is the overlap between the particles, which can be computed as $\delta_{z'i} = R_1 + R_2 - L_i$, where R_1 and R_2 are the radii of both particles and L_i is the distance between their centers (Figure 1b). The overlap in Eq. (4) can also be referred to a stress-free relative position with an initial overlap between spheres, or with

an initial gap (negative overlap), but this is a subject out of the scope of the present paper.

From Eq.(4) we can deduce

$$F_{z'_i} = A_i E \frac{\delta_{z'i}}{L_{0i}} + A_i \nu (\sigma_{x'i} + \sigma_{y'i}) \tag{5}$$

Eq.(5) yields a new expression for the normal contact force which includes an extra second term that brings in the usually missing, but necessary, effect of the particle confinement. Eq.(5) can be rewritten as

$$F_{z'_i} = k_{ni} \delta_{z'i} + A_i \nu (\sigma_{x'i} + \sigma_{y'i}) \tag{6}$$

where k_{ni} is a normal stiffness parameter associated to each pair of particles given by

$$k_{ni} = \frac{A_i E}{L_{0i}} \tag{7}$$

In Eq.(5) $\sigma_{x'i}$ and $\sigma_{y'i}$ are the axial stresses at the contact point in the two orthogonal directions to the normal one. They can be obtained by projecting the stress tensor into those two directions with the associated unit vectors $\hat{e}_{x'}$ and $\hat{e}_{y'}$ as

$$\sigma_{x'i} = \left(\boldsymbol{\sigma} \hat{\boldsymbol{e}}_{x'i} \right)^T \hat{\boldsymbol{e}}_{x'i} \tag{8}$$

$$\sigma_{y'i} = \left(\boldsymbol{\sigma} \hat{\boldsymbol{e}}_{y'i} \right)^T \hat{\boldsymbol{e}}_{y'i} \tag{9}$$

where $\boldsymbol{\sigma}$ is the stress tensor at the contact point. This tensor can be obtained as the average of the stress tensors for the two interacting particles at the ith contact: $\boldsymbol{\sigma}_i = \frac{\boldsymbol{\sigma}_{sphere,0} + \boldsymbol{\sigma}_{sphere,i}}{2}$, where $\boldsymbol{\sigma}_{sphere,k}$ is the stress tensor averaged around the kth sphere and 0 denotes "central sphere". This tensor is typically computed for post-processing the DEM results [12, 13] as

$$\boldsymbol{\sigma}_{sphere} = \frac{1}{V} \sum_{i=1}^{n_c} \boldsymbol{l_i} \otimes \boldsymbol{F_i} \tag{10}$$

where n_c is the number of contacts of the central particle, $\boldsymbol{l_i}$ is the vector connecting the center of the particle to the ith contact point, $\boldsymbol{F_i}$ is the force vector at the ith contact point and V is the volume used to average the stresses. One option is to take $V = V_{sphere}$, where V_{sphere} is the volume of the sphere. A better estimation can be obtained using all the contact areas of the particle with the neighbors as

$$V = \sum_{i=1}^{n_c} \frac{1}{3} A_i \|\boldsymbol{l_i}\| \tag{11}$$

where $A_1, A_2, \ldots, A_n$ are the areas of the contact interfaces.

The stress tensor $\boldsymbol{\sigma}$ can be used in an explicit dynamc solution scheme for the DEM by recovering its expression computed at previous time step. For implicit DEM schemes $\boldsymbol{\sigma}$ has to be computed iteratively within the current time step to get an updated value.

The computation of the contact interface areas A_i is described in Section 3.3.

Remark. Eq.(6) is similar to the typical equation for the normal spring force, adding a new term $(A_i\nu(\sigma_{x'i} + \sigma_{y'i}))$ that accounts for the contribution of the Poisson's effect.

3.2. Tangential forces

From Eq.(2) we can isolate the tangential stresses τ_{ij} as

$$\tau_{ij} = G\gamma_{ij} \tag{12}$$

or

$$\tau_{ij} = G\left(\frac{\partial u_i}{\partial x_j} + \frac{\partial u_j}{\partial x_i}\right) \tag{13}$$

where u_i is the displacement along the ith direction.

Again we can assume that directions i and j are not necessarily oriented with the Cartesian axes. Using the local axes at the contact point (Figure 1a) we obtain:

$$\begin{aligned} \tau_{z'x'} &= G\left(\frac{\partial u_{x'}}{\partial x_{z'}} + \frac{\partial u_{z'}}{\partial x_{x'}}\right) \\ \tau_{z'y'} &= G\left(\frac{\partial u_{y'}}{\partial x_{z'}} + \frac{\partial u_{z'}}{\partial x_{y'}}\right) \end{aligned} \tag{14}$$

In Eqs.(14) the terms $\frac{\partial u_{x'}}{\partial x_{z'}}$ and $\frac{\partial u_{y'}}{\partial x_{z'}}$ can be approximated by $\frac{\delta_{x'i}}{L_i}$ and $\frac{\delta_{y'i}}{L_i}$, respectively, where $\delta_{x'i}$ and $\delta_{y'i}$ are the accumulated relative displacements of the contact point between two particles in the x' and y' directions, respectively, and L_i is the distance between the centers of the spheres (different from L_{0i}, see Figure 1b). Note that $\delta_{x'i}$ and $\delta_{y'i}$ are the lengths of the curves described by the relative tangential displacements over time (see Figure 1b).

The tangential forces at the contact point i, $F_{x'_i}$ and $F_{y'_i}$, can be expressed as:

$$\begin{aligned} F_{x'_i} &= A_iG\left(\frac{\delta_{x'i}}{L_i} + \frac{\partial u_{z'}}{\partial x_{x'}}\right) = k_{ti}\delta_{x'i} + A_iG\frac{\partial u_{z'}}{\partial x_{x'}} \\ F_{y'_i} &= A_iG\left(\frac{\delta_{y'i}}{L_i} + \frac{\partial u_{z'}}{\partial x_{y'}}\right) = k_{ti}\delta_{y'i} + A_iG\frac{\partial u_{z'}}{\partial x_{y'}} \end{aligned} \tag{15}$$

with k_{t_i} being a tangential stiffness parameter associated to the ith contact point between each pair of particles, whose value is

$$k_{ti} = \frac{A_iG}{L_i} \tag{16}$$

The terms $\frac{\partial u_{z'}}{\partial x_{x'}}$ and $\frac{\partial u_{z'}}{\partial x_{y'}}$ in Eqs.(14) cannot be obtained with the information provided by the pair of particles in contact. They can be deduced, however, from the information contained in the stress tensor, which is fed by information from all the surrounding particles. Using Eq.(13), and choosing the local axes at the contact point, we can write:

$$
\begin{aligned}
\left(\frac{\partial u_{z'}}{\partial x_{x'}} \right)_{i,step} &= \left(\frac{\tau_{z'x',i}}{G} - \frac{\delta_{x'i}}{L_i} \right)_{step} \\
\left(\frac{\partial u_{z'}}{\partial x_{y'}} \right)_{i,step} &= \left(\frac{\tau_{z'y',i}}{G} - \frac{\delta_{y'i}}{L_i} \right)_{step}
\end{aligned}
\tag{17}
$$

Sub-index *step* in Eqs.(17) denotes the time step at which the different terms are approximated. For explicit dynamic solution schemes, *step* refers to the previous step. For implicit schemes, *step* refers to the current time step and the term is updated iteratively.

The tangential forces can be finally written as

$$
\begin{aligned}
F_{x'_i} &= k_{ti}\delta_{x'i} + A_i G \left(\frac{\tau_{z'x',i}}{G} - \frac{\delta_{x'i}}{L_i} \right)_{step} \\
F_{y'_i} &= k_{ti}\delta_{y'i} + A_i G \left(\frac{\tau_{z'y',i}}{G} - \frac{\delta_{y'i}}{L_i} \right)_{step}
\end{aligned}
\tag{18}
$$

where $\tau_{z'x',i}$ and $\tau_{z'y',i}$ are the tangential components of the stress tensor in local coordinates, $\boldsymbol{\sigma}'_i$. This tensor is computed by rotating the standard stress tensor $\boldsymbol{\sigma}_i$ (in global coordinates) as:

$$
\boldsymbol{\sigma}'_i = \boldsymbol{R}_i^T \boldsymbol{\sigma}_i \boldsymbol{R}_i
\tag{19}
$$

where $\boldsymbol{R}_i$ is the rotation matrix between the Cartesian and the local axes of contact i.

Remark. Note that Eq.(19) is an extension of the usual expression for the tangential forces in the DEM by adding an extra term that accounts for the surroundings of the bond.

3.3. The contact area between two spheres

In Sections 3.1 and 3.2, the contact interface area A is an important value that affects the contact force and, hence, the global response of the modeled material in terms of apparent (macro) Young's modulus and Poisson's ratio values. Some authors [8, 11] have provided estimations of A_i for linear elastic contact laws taking into account the radii of the contacting spheres. Some typical options are:

- A is taken as the area associated to the minimum radius between two particles: $2R_{min}$ in 2D or πR_{min}^2 in 3D.
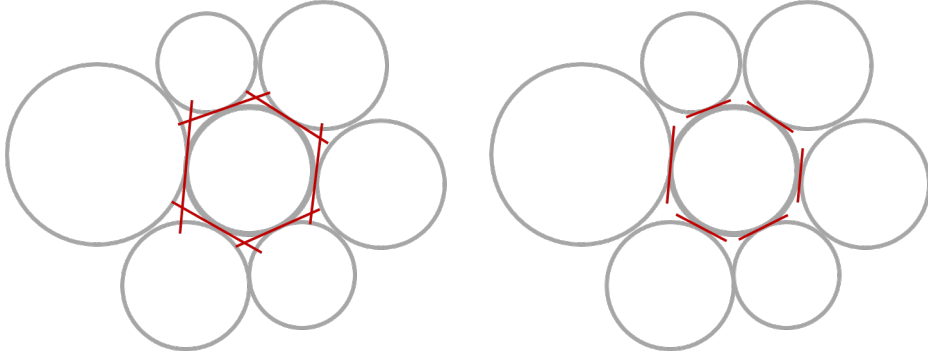
Figure 2: Scheme of overlapping contact areas (left) and gaps between contact areas (right)

- A is taken as the area associated to an average radius between two particles: $2R_{av}$ in 2D or πR_{av}^2 in 3D (with $R_{av} = \frac{R_1 + R_2}{R_1 R_2}$, for example).

Most of these estimations do not take into account that too big values of A_i introduce an overlap between contacts, or that too small values of A represent gaps between contacts. Figure 2 shows a scheme of both cases.

In this work we propose a way to calculate the contact areas A_i which is based on the concept of Weighted Voronoï Diagram (WVD) (Power Diagram type [14]). In a WVD the faces of each polyhedron are the contact areas. These areas have no overlaps, do not present gaps and can be used for the DEM in order to simulate a continuum. However, building the WVD is computationally expensive, and this goes against the necessary need of performance for the DEM. In this section we give a useful alternative for the approximate computation of the contact area.

Given a set of areas $A_1, A_2, \ldots, A_n$ for the contacting neighbors of a particle, and assuming that these areas take into account the different element sizes, the sum of $\sum_{i=1}^{n} A_i = A_{total}$ should be equal to the sum of the faces areas of the polyhedron given by the WVD ($A_{total,exact}$). This polyhedron is unknown (unless the WVD is generated) but an approximation to its total surface can be roughly estimated by assuming that it is a polyhedron circumscribed to the sphere. So, $A_{total,exact}^{estimation}$ must be bigger that the sphere's surface, i.e.

$$A_{total,exact}^{estimation} \geq 4\pi R^2 = A_{sphere} \tag{20}$$

Using the critical case $A_{total,exact}^{estimation} = 4\pi R^2$ the contact interface areas can be corrected as:

$$A_i^* = A_i \frac{4\pi R^2}{A_{total}} \tag{21}$$

These corrected areas are typically too small and the response of the material is usually softer than wanted. A better estimation for the surface of the polyhedron can be obtained by the following expression:

$$A_{polyhedron} = \alpha A_{sphere} \tag{22}$$

7

number of faces	α
4	3.30797
6	1.90986
8	1.65399
12	1.32503
20	1.20657

Table 1: Value of $\alpha = \frac{A_{polyhedron}}{A_{sphere}}$ for regular polyhedra tangent to a sphere for different numbers of faces
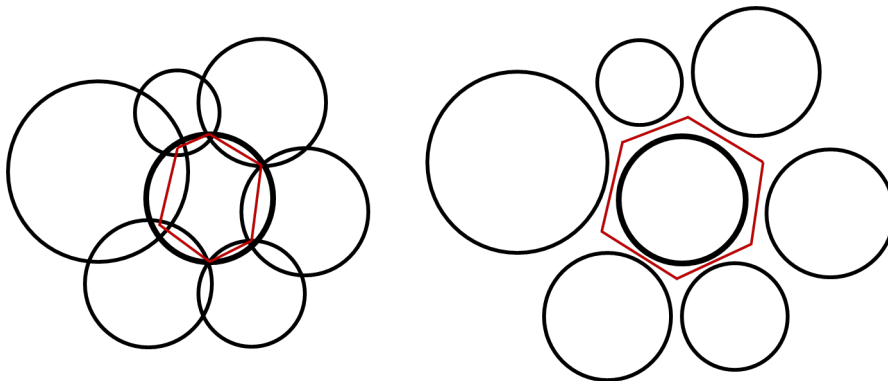

Figure 3: 2D scheme of overlapping (left) and separated (right) particles

where α depends on the number of faces of the polyhedron (number of neighbors of the sphere) and the dispersion in areas of those faces. For regular polyhedra, α is known and the values can be seen in Table 1.

If the number of faces does not allow the formation of a regular polyhedron, α is interpolated from Table 1.

Finally,

$$A_i^* = \alpha 4\pi R^2 \frac{A_i}{A_{total}} \tag{23}$$

The new contact area A_i^* replaces A_i in the corresponding equations of Sections 3.1 and 3.2.

In Eq.(23) the possible irregularity of the polyhedron, even in the cases with 4,6,8,12 or 20 faces is not taken into account. Extra adjustments can be introduced by using more correction coefficients.

Further corrections for the contact areas

Eq.(23) yields accurate results as long as the spheres are tangent. However, it is very common to work with packings of spheres where the spheres are not perfectly tangent and they can present gaps or overlaps, but they can be still considered neighbours (Figure 3).

In these cases the virtual polyhedron would not be tangent to the sphere, and the radius used for calculating A_{sphere} should no longer be the actual radius of the sphere, R. Instead, it can be replaced by

$$R^* = \frac{\sum_{i=1}^{n_c} \left(R - \frac{\gamma_i}{2} \right)}{n_c} \tag{24}$$

with γ_i being the overlap of the sphere with neighbor i (a negative value means a gap between spheres). The value of R^* replaces R in Eq.(23).

4. Results

4.1. Methodology validation

Several numerical tests have been carried out in order to validate this theoretical framework. These simulations were addressed to find out the ability of the method for capturing the elastic behavior of a given specimen using the explicit version of the DEM. The sample studied is a cubic volume of side 0.5 m. The specimen was tested for a Young's modulus of $E = 1.0e9$ Pa and two different Poisson's ratio values of $\nu = 0.2$ and $\nu = 0.35$. All computations with the DEM using $\nu \geq 0.5$ were instable and the sample exploded.

The elastic response of the sample was obtained via a UCS test by imposing constant and confronting velocities in the Z axis to the spheres at the top and bottom of the specimen, while allowing the free movement in the XY plane.

Three packing typologies were tested: cartesian packing, staggered packing and random packing. The average coordination number of the cartesian mesh was 6, while for the staggered and the random was 13 and 11 respectively. The porosity of the random mesh was 0.25. Details on the studied geometries are given next:

1. The cartesian packing had 132651 spheres of 1 cm of diameter (Figure 4). For this configuration, all contacts are either vertical (aligned with Z) or horizontal (aligned with X or Y).

2. The staggered packing had 33201 spheres of 2 cm of diameter (Figure 5). This configuration, also called 'body centered cube' presents a bigger density of contacts, and still can be considered 'structured', as the same cell is replicated in the X, Y and Z directions.

3. A random packing was generated with 11511 spheres of an average diameter of 2 cm (Figure 6).
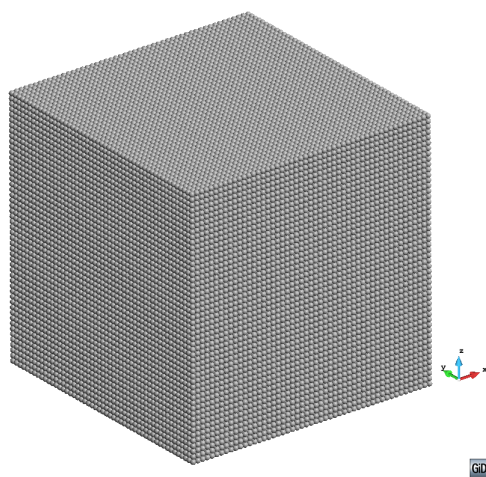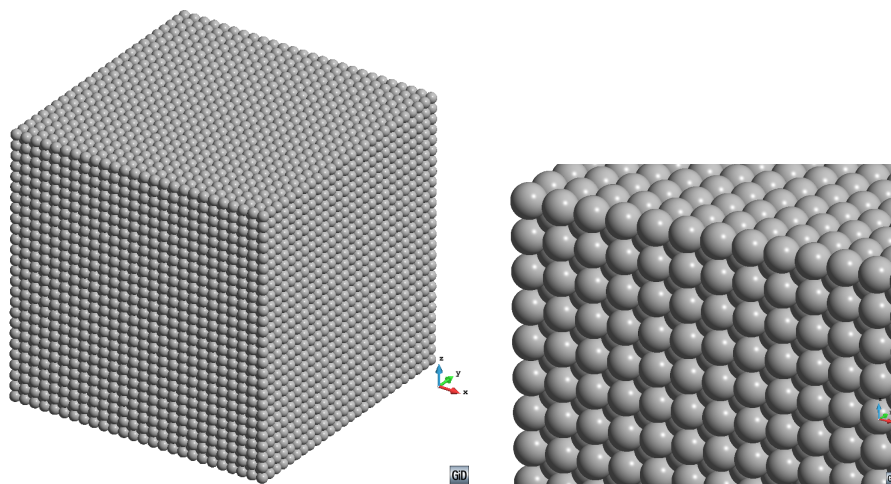
Figure 4: Cartesian packing of 132651 spheres.

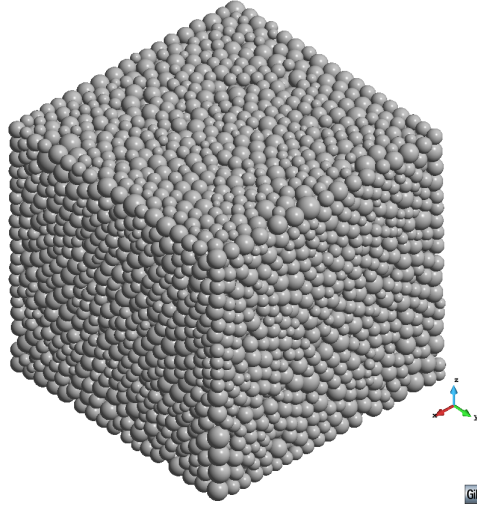Figure 5: Staggered packing of 33201 spheres. Global view (left) and detail (right)

Figure 6: Random packing of 11511 spheres

4.2. Measurement of the macro values of E and ν for the samples

The macro Young's modulus (E_{macro}) was computed as the quotient between the stress at the moving boundaries (top layer and bottom layer) over the total vertical strain of the specimen. The stress at the boundaries was calculated as the sum of the reaction forces over the spheres of the top layer divided by the section area of the specimen

$$E_{macro} = \frac{\sigma_{computed}}{\varepsilon_z} = \frac{\sum_{i=1}^{n_s} F_{react,i}}{\varepsilon_z} \tag{25}$$

where n_s is the number of spheres of the top layer, $F_{react,i}$ is the reaction force on the ith sphere and ε_z is the vertical strain of the specimen (enforced in the form of imposed displacements).

The macro Poisson's ratio ν_{macro} for the sample was computed as the quotient of the horizontal strain over the vertical strain. Both strains were measured on the longest diagonal in the cube, or the straight line connecting the centers of the two most distant spheres in the sample. An alternative to this measurement is to compute the average of ν for all the bonds connecting the centers of every pair of spheres in contact within the specimen. In any case, the expression used to compute the macro Poisson's ratio between any two centers of spheres C1 and C2 in the sample is

$$\nu_{macro} = -\frac{\varepsilon_{xy}}{\varepsilon_z} = -\frac{1 - \frac{d_{xy,in}}{d_{xy,fin}}}{1 - \frac{d_{z,in}}{d_{z,fin}}} \tag{26}$$

where ε_{xy} is the horizontal strain of the measured line, d_{xy} is the horizontal projection of the line length, d_z is the vertical projection of that length and subindices *initial* and *final* denote if the measure is taken before or after the deformation, respectively.
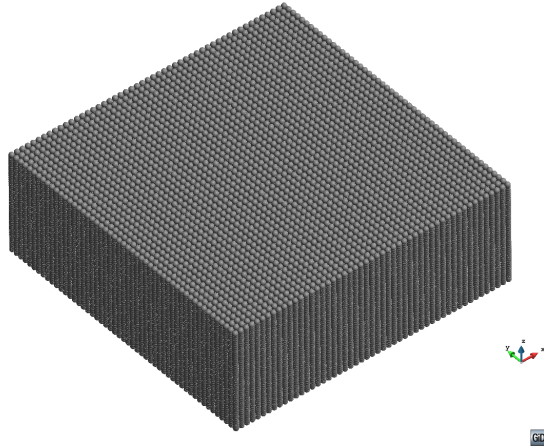
11

Figure 7: Deformed sample for a cartesian packing. Displacement amplified by a factor of 3.0e4.

4.3. Analysis and comparison of the results

The results shown in this section did not require any calibration effort and were obtained in a single run with the specified input parameters.

Cartesian packing

A very good result was obtained for the Young's modulus value, with an error of -0.6%. On the other hand, the errors in computing the macro Poisson's ratios corresponding to prescribed values of $\nu = 0.2$ and $\nu = 0.35$ were 1.45% and -0.22%, respectively. For this particular case the Poisson's ratio averaged over all the contacts makes no sense as the bonds between spheres experiment no rotation, so no measure of the macro Poisson's ratio is possible. Figure 7 shows the deformation of the cartesian mesh with a scaling factor of 3.0e4.

Staggered packing

A very good result was obtained for the Young's modulus, with an error of 0.7%. Very good values were also obtained for the macro Poisson's ratios, with 0.4% and -2.9% errors for the prescribed values of $\nu = 0.2$ and $\nu = 0.35$, respectively. It is worth noting that in this case we are referring to the average value for ν (Figure 8), which is very well fitted and a good representation of the whole specimen, since all the bonds in the sample present the same angle with respect to the XY plane. A small expansion can be observed at the top and bottom of the specimen that can be explained as a result of a lower stiffness of the spheres at the outer layers. Figure 8 shows the deformed configuration of the sample using a scaling factor of 3.0e4. Finally, Figure 9 shows the Poisson's ratio field. It can be clearly observed that the field in the interior of the sample is very uniform with
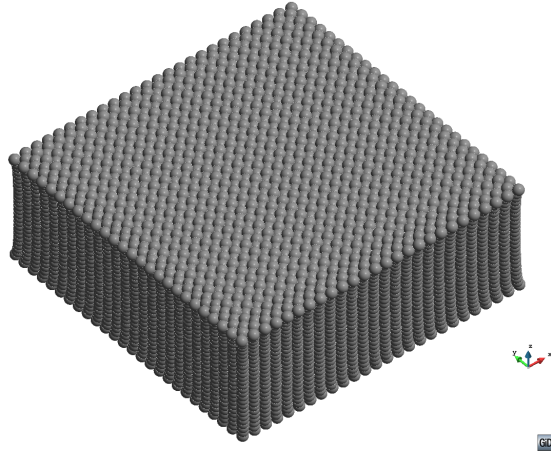
12

Figure 8: Deformed sample for a staggered packing. Displacement amplified by a factor of 3.0e4

an average value of around $\nu = 0.2$, this being the exact Poisson's ratio specified for this case.

Random packing

Again, a very good value of the Young's modulus is obtained (only a 1.2% smaller than the theoretical value). The results obtained in measuring the macro Poisson's ratio for $\nu = 0.2$ and $\nu = 0.35$ were -3% and -5.1%, respectively. Figure 10 shows the deformed mesh using an enlargement factor of 3e4. Note that the random packing introduces a high heterogeneity in the behavior of the sample, but still the results for the elastic contact are very satisfactory.

Comparison of the results obtained with the conventional DEM contact law

The previous numerical experiments were run with the terms that add the Poisson's effect (Section 3.1) and an extra tangential force (Section 3.2). In this section we will show that not adding those contributions results in the Poisson's effect not getting properly captured and to Young's modulus values ranging from 20 to 25% smaller than the theoretical ones. Using the conventional contact laws for the DEM, the results for the staggered and random meshes are very similar. For a Poisson's ratio of $\nu = 0.2$, the error in the computation of the Young's modulus for both geometries is about -21%, while for a Poisson's ratio equal to $\nu = 0.35$, the error for E in both meshes is around -24%. The error for capturing a Poisson's ratio of $\nu = 0.2$ is about -40% for both meshes, while for the $\nu = 0.35$ the response gets worse and the error increases to -63%. On the other hand, the cartesian mesh is capable of computing the correct value of the Young's modulus with the same accuracy as in the previous tests. The reason is that the new force
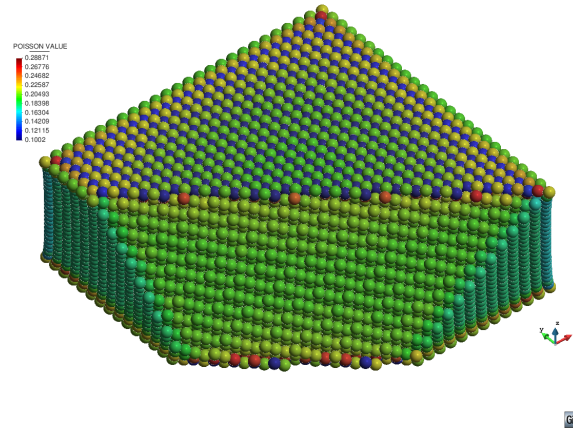
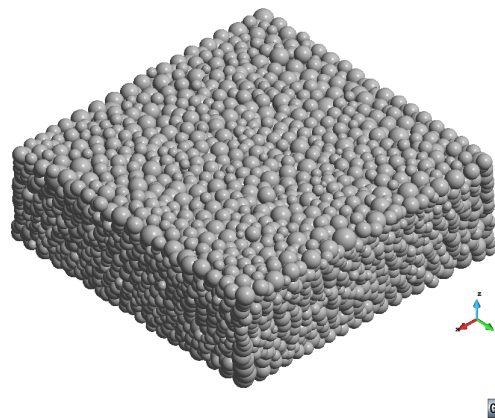Figure 9: Poisson's ratio values for an input value of $\nu = 0.2$

Figure 10: Deformed sample for a random packing. Displacement amplified by a factor of 3.0e4

14

Input parameters: $E = 1.0e9$, $\nu = 0.2$						
Error in computed values	Cartesian packing		Staggered packing		Random packing	
Young's modulus	Standard DEM	Improved DEM	Standard DEM	Improved DEM	Standard DEM	Improved DEM
Poisson's ratio E	-0.6 %	-0.6 %	-20.8 %	0.7 %	-22.0 %	-1.2 %
Poisson's ratio ν	-100.0 %	1.45 %	-43.0 %	+0.4 %	-29.0 %	-3.0 %

Table 2: Effect of adding the extra terms in the normal and tangential contact forces

Input parameters: $E = 1.0e9$, $\nu = 0.35$						
	Cartesian packing		Staggered packing		Random packing	
	Standard DEM	Improved DEM	Standard DEM	Improved DEM	Standard DEM	Improved DEM
Poisson's ratio E	-0.6 %	-0.6 %	-23.0 %	0.7 %	-24.5 %	-1.2 %
Poisson's ratio ν	-100.0 %	0.22 %	-64.0 %	-2.9 %	-63.0 %	-5.1 %

Table 3: Effect of adding the extra terms in the normal and tangential contac forces

terms, and in particular the term related to the contribution of the shear strains parallel to the bonds, do not affect the calculation of E when the mesh is cartesian, as it can be inferred from the theoretical section. Finally, deactivating the term that adds the Poisson's effect yields a computed value of $\nu = 0$ for both $\nu = 0.2$ and $\nu = 0.35$ targets. This is a logical and expected result taking into account the non-existence of forces in the XY plane (the only ones that would cause strains in that direction) in a cartesian specimen subjected to stresses in the Z axis. Tables 2 and 3 compare the errors obtained with both methods for the same input values of E and ν, where 'improved DEM' stands for the formulation presented in this work for computing the contact forces, while 'standard DEM' denotes results without the extra terms for the force-displacement relationship presented in Sections 3.1 and 3.2.

5. Conclusions

A modification of the contact laws between particles has been proposed in order to improve the elastic behaviour of a packing of spheres when trying to model a continuum with the DEM.

The newly added terms in Eqs.(6) and (18) complete the conventional forces of the cohesive DEM traditionally used to model materials like rocks or cement. These terms notably improve the elastic response of the modeled material versus the conventional approach and avoid the need of any calibration process if the contact areas are calculated using the methodology explained in Section 3.3.

The modified contact laws here proposed yield the same results regardless of the type of packing (cartesian, staggered or random) or the coordination number. Also the error in the computed value of the elastic parameters for an elastic sample (E and ν) did not show any dependency on the particular values of E or ν.
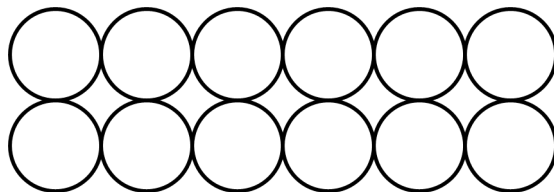
Figure 11: Two layers of a Cartesian packing of particles

Appendix A. Shortcomings of the classic DEM when trying to reproduce the Young's modulus

In order to emphasize the importance of the extra terms proposed in the constitutive expressions of Sections 3.1 and 3.2, an example is shown to evidence some shortcomings of the classical DEM for cohesive materials:

Let us enforce a vertical strain of $\varepsilon_v = \frac{\delta_v}{L_{0v}}$ on two layers of circles, where δ_v is the relative vertical displacement between the layers and L_{0v} is the initial vertical distance between the layers (distance between centers).

Case 1
In a Cartesian arrangement (Figure 11), a two-layer sample formed by circles can be taken as a representative cell (Figure 12). Let us impose a descending displacement δ_v to the upper layer, while keeping the lower layer fixed. L_{0v} is then equal to $2R$, so the vertical strain has a value of $\varepsilon = \frac{\delta_v}{L_{0v}} = \frac{\delta_v}{2R}$.

In the standard DEM, the vertical force between these two circles is $F_v = k_n \delta_v$, where k_n is a fixed, calibrated value, or is obtained by $k_n = \frac{EA}{2R} = \frac{E2R}{2R} = E$. Let us choose the latter, where the contact area A has been assumed to be $2R$ for this case, which is a value that ensures that the sum of all areas between both layers is equal to the whole section, without gaps or overlaps.
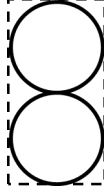
Figure 12: Representative cell of the Cartesian packing for vertical force analysis
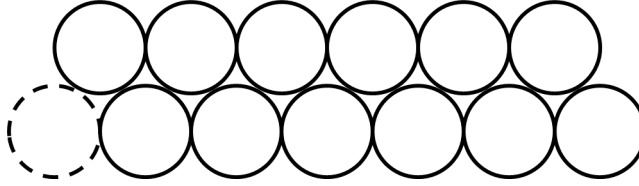

Figure 13: Two layers of a dense, structured packing of particles

Case 2

In a structured dense packing of circles (Figure 13), a sample of one upper circle and two halves of lower circles can be taken a a representative cell (Figure 14). In order to impose the same vertical strain, let us impose a descending displacement $\delta_v^* = \delta_v \cos \theta$ and $L_{0v}^* = 2R \cos \theta$. With this configuration, the vertical strain is $\varepsilon^* = \frac{\delta_v^*}{L_{0v}^*} = \frac{\delta_v \cos \theta}{2R \cos \theta} = \frac{\delta_v}{2R} = \varepsilon$.

In the classical DEM, the vertical force acting on the upper circle is:

$$F_v^* = 2 \left(F_n^* \cos \theta + F_t^* \sin \theta \right) \tag{27}$$

where F_n^* and F_t^* are the normal and tangential forces between the upper circle and one of the lower ones.

Using the concepts of the classical DEM, these two forces can be written as a stiffness constant multiplying a relative displacement, i.e.

$$F_v^* = 2 \left(k_n \delta_{v,n}^* \cos \theta + k_t \delta_{v,t}^* \sin \theta \right) \tag{28}$$

where $\delta_{v,n}^*$ is the relative normal displacement at the contact point and $\delta_{v,t}^*$ is its tangential counterpart. In Eq.(28) k_n is a fixed calibrated value, or it is obtained by $k_n = \frac{EA^*}{2R}$. Also in Eq.(28) k_t is usually taken as a fraction of k_n, but it can also be estimated as $k_t = \frac{GA^*}{2R}$. No matter which option
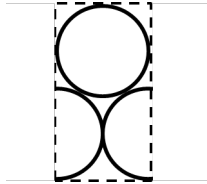

Figure 14: Representative cell of the dense packing for vertical force analysis

is chosen, in general $k_n \neq k_t$. For further developments we have chosen the second choice for defining k_n. Then, the expression of the total vertical force on the upper circle is:

$$F_v^* = 2 \left(\frac{EA^*}{2R} \delta_v^* \cos^2 \theta + \frac{GA^*}{2R} \delta_v^* \sin^2 \theta \right) \tag{29}$$

Taking into account that $A^* = \frac{A}{2} \frac{1}{\cos \theta} = \frac{R}{\cos \theta}$ and $\delta_v^* = \delta_v \cos \theta$ we finally obtain:

$$F_v^* = E\delta_v \cos^2 \theta + G\delta_v \sin^2 \theta \tag{30}$$

Comparison

In both cases, the total horizontal contact area is $2R$ (in Case 2, the two contact areas must be projected to the horizontal direction to recover this value). Having the same vertical strain in both cases, the vertical stress should be equal as well, understanding the vertical stress as the vertical force divided by the total area. Since the area is the same, the vertical forces must be equal. However, $F_v^* \neq F_v$ in general. They can only be equal if we assume that $G = E$. In other words, k_t must be equal to k_n in order to recover the same vertical stiffness.

Conclusion

From the above exercise we conclude that the micro parameters used in the standard DEM (k_n and k_t) yield different stiffness values for a sample depending on the position of the particles, or the direction of the bonds. This means that a random packing of spheres modeled with the standard DEM is extremely heterogeneous in terms of internal stiffness. It also means that a calibration obtained for one sample is not necessarily useful for other samples, as most probably the orientation of the bonds will be different.

Appendix B. Dynamics of the DEM and mass adjustment

When the cohesive DEM is used to model a continuum, any dynamic response is directly linked to the mass of the particle (a circle in 2D, and a sphere in 3D). However, the voids between particles are not typically considered. The computed sample is too porous, less dense than the real one, and the dynamic waves travel faster than expected.

In order to get a better approximation to the actual mass associated to each particle, the volume of the voids should be distributed among the neighbor particles. Instead of doing this, the volume of the particle can be computed by the 'representative volume' expressed by of Eq.(11). Multiplying this volume by the bulk density of the material yields a mass for the particle which allows a better capture of any dynamic wave in the modeled continuum.

References

[1] Cundall PA, Strack OD (1979) A discrete numerical model for granular assemblies. Geotechnique 29(1):47–65

[2] Langston PA, Tüzün U, Heyes D M (1995) Discrete element simulation of granular flow in 2D and 3D hoppers: dependence of discharge rate and wall stress on particle interactions. Chemical Engineering Science 50(6):967–987

[3] Cleary P W, Sawley ML (2002) DEM modelling of industrial granular flows: 3D case studies and the effect of particle shape on hopper discharge. Applied Mathematical Modelling 26(2):89–111

[4] Xu BH, Yu AB (1997) Numerical simulation of the gas-solid flow in a fluidized bed by combining discrete particle method with computational fluid dynamics. Chemical Engineering Science 52(16):2785–2809

[5] Tsuji Y, Kawaguchi T, Tanaka T (1993) Discrete particle simulation of two-dimensional fluidized bed. Powder technology 77(1):79–87

[6] Oñate E, Labra C, Zárate F, Rojek J (2012) Modelling and simulation of the effect of blast loading on structures using an adaptive blending of discrete and finite element methods. Risk Analysis, Dam Safety, Dam Security and Critical Infrastructure Management, Chapter 53:365–372.

[7] Moreno R, Ghadiri M, Antony SJ (2003) Effect of the impact angle on the breakage of agglomerates: a numerical study using DEM. Powder Technology 130(1):132–137

[8] Oñate E, Zárate F, Miquel J, Santasusana M, Celigueta MA, Arrufat F, Gandikota R, Valiullin KM, Ring L (2015) A local constitutive model for the discrete element method. Application to geomaterials and concrete. Computational Particle Mechanics 2(2):139–160.

[9] Brown NJ, Chen JF, Ooi JY (2014) A bond model for DEM simulation of cementitious materials and deformable structures. Granular Matter 16(3):299–311

[10] Hentz S, Daudeville L, Donzé FV (2004) Identification and validation of a discrete element model for concrete. Journal of engineering mechanics 130(6):709–719

[11] Labra CA (2012) Advances in the development of the discrete element method for excavation processes. PhD Thesis, Universitat Politècnica de Catalunya, Barcelona

[12] Luding S (2008) Introduction to discrete element methods: basic of contact force models and how to perform the micro-macro transition to continuum theory. European Journal of Environmental and Civil Engineering 12(7-8):785–826

[13] Rojek J, Karlis GF, Malinowski LJ, Beer G (2013) Setting up virgin stress conditions in discrete element models. Computers and Geotechnics 48:228–248

[14] Okabe A, Boots B, Sugihara K, Chiu SN (2009) Spatial tessellations: concepts and applications of Voronoi diagrams, Vol. 501, John Wiley & Sons

[15] Dadvand P, Rossi R, Oñate E (2010) An object-oriented environment for developing finite element codes for multi-disciplinary applications. Archives of computational methods in engineering 17(3):253–297

[16] www.cimne.com/dempack

[17] Ribó R, Pasenau M, Escolano E, Ronda JS, González LF (1998) GiD reference manual. CIMNE, Barcelona

[18] Rojek J, Oñate E, Labra C, Kargl H (2011). Discrete element simulation of rock cutting. International Journal of Rock Mechanics and Mining Sciences 48(6):996–1010

[19] Oñate E, Rojek J (2004) Combination of discrete element and finite element methods for dynamic analysis of geomechanics problems. Computer methods in applied mechanics and engineering 193(27):3087–3128